





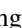




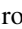



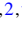


## Synthesis and electronic characterization of $\text{Nd}_{2-x}\text{Sr}_x\text{NiO}_4$ thin films ( $0 \leq x \leq 1.4$ )

Nicole K. Taylor <sup>1,\*</sup>, Dan Ferenc Segedin <sup>2,\*</sup>, Ari B. Turkiewicz <sup>2</sup>, Yang Zhang <sup>3</sup>, Spencer T. Doyle <sup>2</sup>, Grace A. Pan <sup>2</sup>, Haoyue Jiang <sup>4,5</sup>, Aaron Bostwick <sup>6</sup>, Chris Jozwiak <sup>6</sup>, Eli Rotenberg <sup>6</sup>, Alessandra Lanzara <sup>4,7</sup>, Ismail El Baggari <sup>3</sup>, Charles M. Brooks <sup>2</sup>, Alpha T. N'Diaye <sup>6</sup>, Luca Moreschini <sup>4,7</sup> and Julia A. Mundy <sup>1,2,†</sup>

<sup>1</sup>*School of Engineering and Applied Science, Harvard University, Cambridge, Massachusetts 02138, USA*

<sup>2</sup>*Department of Physics, Harvard University, Cambridge, Massachusetts 02138, USA*

<sup>3</sup>*The Rowland Institute at Harvard, Harvard University, Cambridge, Massachusetts 02142, USA*

<sup>4</sup>*Department of Physics, University of California at Berkeley, Berkeley, California 94720, USA*

<sup>5</sup>*Applied Science and Technology, University of California, Berkeley, California 94720, USA*

<sup>6</sup>*Advanced Light Source, Lawrence Berkeley National Laboratory, Berkeley, California 94720, USA*

<sup>7</sup>*Materials Sciences Division, Lawrence Berkeley National Laboratory, Berkeley, California 94720, USA*



(Received 19 August 2024; accepted 3 February 2025; published 7 March 2025)

Layered nickelates have been studied extensively over the last three decades due to their structural similarities to the high- $T_c$  superconducting cuprates. Using reactive oxide molecular beam epitaxy (MBE), we synthesize  $\text{Nd}_{2-x}\text{Sr}_x\text{NiO}_4$  thin films for  $x = 0 - 1.4$  to probe the properties and electronic structure as a function of hole doping. The samples with lower doping show semiconducting behavior across the temperatures probed with an onset of metallic conductivity at  $x = 1.4$ . We also present polarization-dependent O  $K$  and Ni  $L_{2,3}$  x-ray absorption spectra to track the evolution of the oxygen-nickel hybridization, distribution of holes between O  $2p$  and Ni  $3d$  states and the nickel oxidation state across the series. Angle-resolved photoemission spectroscopy (ARPES) measurements reveal a Fermi surface that comprises a cupratelike hole pocket of  $d_{x^2-y^2}$  character with an additional electron pocket of  $d_{3z^2-r^2}$  character at  $\Gamma$ . The emergence of a quasiparticle peak at the Fermi vector for  $x = 1.4$  corroborates the insulator-to-metal transition at  $x \sim 1$ . Finally, observe a fully two-dimensional Fermi surface with no momentum-dependent pseudogap, in contrast to measurements of the related bulk compound,  $\text{Eu}_{0.9}\text{Sr}_{1.1}\text{NiO}_4$ .

DOI: [10.1103/PhysRevMaterials.9.L032001](https://doi.org/10.1103/PhysRevMaterials.9.L032001)

**Introduction.** The layered nickelates,  $R_{2-x}\text{Sr}_x\text{NiO}_4$  ( $R = \text{La, Nd, Eu, } \dots$ ), are a highly correlated system that show a number of emergent phenomena [1–4]. These materials have been extensively studied, particularly since they are isostructural to the high-temperature superconductor,  $\text{La}_{2-x}\text{Sr}_x\text{CuO}_4$  [5,6], as shown in Fig. 1(a). Metallicity and subsequently superconductivity can be realized in the layered cuprates with only a few percent of strontium doping at the rare-earth site [7]. In contrast, the  $R_{2-x}\text{Sr}_x\text{NiO}_4$  compounds do not reach a metallic state until  $\sim 50\%$  hole doping on the rare-earth site ( $x_c \sim 1.0$ ) [8,9]. Despite the high doping required to realize a conducting state and the absence of superconductivity, the layered nickelates remain close analogues to the cuprates.  $\text{Eu}_{0.9}\text{Sr}_{1.1}\text{NiO}_4$  exhibits an electronic structure with striking similarities to the cuprates, including Fermi arcs and a momentum-dependent pseudogap [10]. The robust insulating phase of the layered nickelates at low doping exhibits charge ordering [11,12], charge/spin stripes [12–14], and antiferromagnetic ordering at low temperatures [15]. The hole-doped  $R_{2-x}\text{Sr}_x\text{NiO}_4$  compounds are also an appealing analog to the bilayer  $\text{La}_3\text{Ni}_2\text{O}_7$  that has been recently shown to superconduct under high pressure [16];  $R_{1.5}\text{Sr}_{0.5}\text{NiO}_4$  has the same

nickel  $d^{7.5}$  filling as  $\text{La}_3\text{Ni}_2\text{O}_7$ , and charge order which can be suppressed with strontium doping.

Despite interest in this family of compounds, layered nickelates have been primarily synthesized in the bulk crystal form [17–19]. It is particularly appealing to explore these materials in the thin film geometry [9,17,18,20], where epitaxial strain could further tune the ground state [21]. In contrast to extensive spectroscopic studies of the bulk crystals [12,22–25], the thin film work to date has primarily focused on the electric properties [9,17,18,20]. That said, there remain challenges in the synthesis of these compounds, particularly with high strontium concentrations, both in the thin-film and bulk crystal form. To successfully hole dope the layered nickelates, the state of nickel oxidation must be pushed beyond a  $\text{Ni}^{2+}$  valence state in the parent  $R_2\text{NiO}_4$  compound toward a nominally unstable  $\text{Ni}^{4+}$  state in the highly doped compounds [26].

Here we report the synthesis of the layered nickelate compounds using reactive oxide MBE, successfully synthesizing  $\text{Nd}_{2-x}\text{Sr}_x\text{NiO}_4$  thin films for  $x = 0 - 1.4$  under  $\sim 0.9\%$  compressive strain on  $\text{LaAlO}_3$ . We use distilled ozone ( $\text{O}_3$ ) to realize high oxidation states of the nickel cation. By altering the strontium content,  $x$ , we probe the phase diagram of these materials, observing a transition from semiconducting for  $x \leq 1$  to a metallic state for  $x = 1.4$ . We provide a comprehensive analysis of the electronic structure of these materials by analyzing the polarized and polarized-averaged x-ray absorption spectra, while simultaneously tracking the

\*These authors contributed equally to this work.

†Contact author: [mundy@fas.harvard.edu](mailto:mundy@fas.harvard.edu)

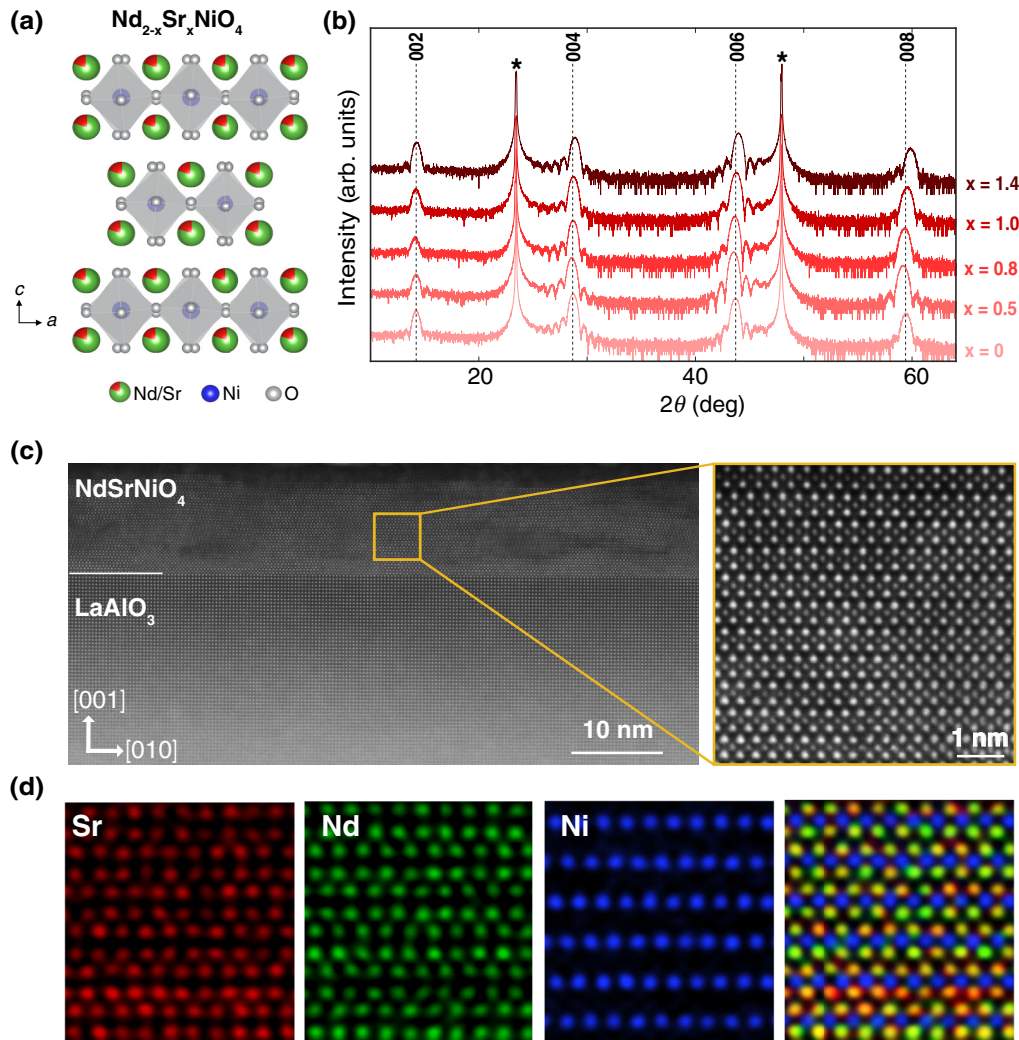


FIG. 1. Structural characterization of  $\text{Nd}_{2-x}\text{Sr}_x\text{NiO}_4$  on  $\text{LaAlO}_3$  (100). (a) Schematic crystal structure of  $\text{Nd}_{2-x}\text{Sr}_x\text{NiO}_4$ . (b) X-ray diffraction scans of  $\text{Nd}_{2-x}\text{Sr}_x\text{NiO}_4$  for  $x = 0, 0.5, 0.8, 1.0,$  and  $1.4$ . The asterisks denote  $\text{LaAlO}_3$  substrate peaks and the vertical dotted lines denote the  $00l$  peak positions of the undoped  $\text{Nd}_2\text{NiO}_4$  thin film. (c) Large field of view and zoom-in HAADF-STEM image of  $\text{NdSrNiO}_4$  ( $x = 1.0$ ). (d) Atomic-resolved EDS mapping of the  $x = 1$  sample shows the homogeneous distribution of doped strontium. The neodymium, strontium and nickel signals are represented by red, green, and blue, respectively.

nickel valence state and hole occupation of both the Ni  $L_{2,3}$  edge and O  $K$  edge. Further characterization with angle-resolved photoemission spectroscopy (ARPES) reveals a fully two-dimensional Fermi surface for  $\text{Nd}_{0.6}\text{Sr}_{1.4}\text{NiO}_4$  consistent with density functional theory (DFT) calculations for paramagnetic  $\text{La}_2\text{NiO}_4$  [27]. This behavior contrasts with the more three-dimensional Fermi surface observed in  $\text{Eu}_{0.9}\text{Sr}_{1.1}\text{NiO}_4$  [28]. Finally, we do not observe a momentum-dependent pseudogap, as reported for bulk  $\text{Eu}_{0.9}\text{Sr}_{1.1}\text{NiO}_4$  [10].

#### Experimental methods.

*a. Thin-film synthesis via molecular beam epitaxy.* We synthesize  $\text{Nd}_{2-x}\text{Sr}_x\text{NiO}_4$  on  $\text{LaAlO}_3$  (100) films from  $x = 0$  to  $x = 1.4$  using a Riber Compact21 ozone-assisted molecular beam epitaxy system. High quality  $\text{Nd}_{n+1}\text{Ni}_n\text{O}_{3n+1}$  Ruddlesden-Popper nickelate films have been previously synthesized on  $\text{LaAlO}_3$  (100) substrates [29,30]. Here we synthesize the  $\text{Nd}_{2-x}\text{Sr}_x\text{NiO}_4$  (the  $n = 1$  end member of the Ruddlesden-Popper series) at a  $\sim 890^\circ\text{C}$  nominal substrate temperature and  $1.0 \times 10^{-6}$  Torr  $\text{O}_3$ . The crystalline quality

improves with increasing growth temperature, in accordance with the high temperature stability of  $R_2\text{NiO}_4$  compounds (Fig. S1). The highly oxidizing conditions [30,31] provided by distilled ozone facilitate the synthesis of the doped films where the nominal nickel oxidation state is greater than  $3+$ . The method used to calibrate the neodymium and nickel monolayer shutter times is described in Ref. [29]. To calibrate the strontium monolayer shutter time, we track the reflection high energy electron diffraction (RHEED) oscillations during the shuttered growth of homoepitaxial  $\text{SrTiO}_3$ , as described in [32].

We deposit  $\text{Nd}_{2-x}\text{Sr}_x\text{NiO}_4$  thin films using a shuttered deposition scheme [29–31]. Here, the  $A$ -site cations, strontium and neodymium, are deposited simultaneously for the duration of the neodymium dose; the remainder of the strontium is deposited if needed to reach the intended doping. The  $B$ -site nickel layer is then deposited sequentially following the completion of the  $A$ -site layers. We tune the strontium doping via relative neodymium and strontium subunit cell shutter times to

control the relative dosing. This method allows us to maintain the same cell temperatures throughout the synthesis of the doping series. All films in this study are  $\sim 13$  nm thick.

*b. Structural characterization.* X-ray diffraction (XRD) measurements were made using the Malvern panalytical empyrean diffractometer with Cu  $K\alpha_1$  radiation, ( $\lambda = 1.5406$  Å). We compute the  $c$ -axis lattice constants using Nelson-Riley fits to the x-ray peak positions [33]. Reciprocal space maps (RSM) were taken using the PIXcel3D area detector for  $x = 1.4$  to determine the strain to the LaAlO<sub>3</sub> substrate.

*c. Electron microscopy.* The cross-sectional scanning transmission electron microscopy (STEM) specimens were prepared using standard gallium focused ion beam (Thermo-Fisher Helios) lift out and thinning. The samples were thinned down using an accelerating ion voltage of 30 kV with a decreasing current from 100 pA to 40 pA, and then with a fine polishing process using an accelerating voltage of 5 kV and a current of 41 pA. STEM experiments were performed in an aberration-corrected microscope (Thermo-Fisher Scientific Themis Z G3) operated at 200 kV. High-angle annular dark-field (HAADF-STEM) and annular bright-field (ABF-STEM) images were collected using a 18.9 mrad convergence angle and 50 pA probe current. The collection angles ranged from 89 to 200 mrad for HAADF-STEM and 12–23 mrad for ABF-STEM. To minimize image drift and obtain a high signal-to-noise ratio, fast-acquisition frames were collected. Each frame was acquired with  $2048 \times 2048$  pixels and 200 ns dwell time. Forty frames in total were collected and aligned using a rigid registration method optimized for noisy image frames [34]. The atomic energy dispersive x-ray spectroscopy (EDS) data were collected with 80 pA probe current. The EDS data is processed by Gaussian filtering with sigma equal to four pixels.

*d. Electrical transport.* The electrical resistivity was determined using a six contact Hall bar geometry. To create these devices, aluminum foil was used as a shadow mask and then Cr (5 nm)/Au (100 nm) contacts were evaporated using an electron beam evaporator. To define the Hall bar channels, we scribed the surface of the films with a diamond scribe. The scribed channels include two current leads (source and drain) and four voltage leads measuring the longitudinal and transverse voltage drops. The electrical transport data were acquired using the quantum design physical property measurements system (PPMS) equipped with a 14 T magnet. The longitudinal resistance ( $R_{xx}$ ) as a function of temperature was measured at 0 T at temperatures between 1.8 K and 300 K.

*e. X-ray absorption spectroscopy.* X-ray absorption spectroscopy (XAS) was performed at the Advanced Light Source (ALS), Lawrence Berkeley National Lab, at beamline 4.0.2 ( $x = 0.5, 1.0,$  and  $1.4$ ) and beamline 6.3.1 ( $x = 0$ ). The spectra acquired at both beamlines were taken at 300 K in the electron yield mode. At beamline 6.3.1, all spectra were acquired at normal ( $I_x$ ) and  $30^\circ$  grazing ( $I_z$ ) incidence to the beam with a fixed linear horizontal polarization of photons. Due to geometric effects [35], the grazing incident signal was corrected by applying a geometric correction [35]. At beamline 4.0.2, measurements were acquired at  $20^\circ$  grazing ( $I_z$ ) incidence to the beam with linear horizontally ( $I_z$ ) and vertically ( $I_x$ ) polarized soft x-rays. Energy calibrations can vary between beamlines and thus we used the energy alignment of

the Nd  $M_{4,5}$  spectra as a reference. The spectra we present are all normalized to the incident x-ray flux. In addition, the presented normalized spectra are vertically offset across the respective absorbed edge energies. The presented x-ray linear dichroism (XLD) signals presented are computed by subtracting the polarizations,  $I_z$ - $I_x$  spectra, and averaged over four to eight scans.

*f. ARPES.* ARPES measurements were performed at the MAESTRO beamline at the Advanced Light Source using a Scienta 4000 electron analyzer. The energy resolution is 10–25 meV and the angle resolution is less than  $0.1^\circ$ . The light polarization was set to  $p$  so that when the sample is facing the analyzer slit with the  $a$  axis in the horizontal  $x$  direction, the electric field of the incident photons is even in the  $x$ - $z$  mirror plane containing the surface normal. Therefore, the measurement is sensitive to the  $d_{x^2-y^2}$ ,  $d_{3z^2-r^2}$ , and  $d_{xz}$  orbitals along  $k_x$ . To clean the surface of the films before ARPES measurements, the films were annealed at  $400^\circ\text{C}$  for two hours in  $\sim 1 \times 10^{-5}$  Torr of 10% ozone. We found that directing the ozone nozzle directly toward the sample within  $\sim 5$  mm of the film surface was essential to ensure no loss of oxygen content and high data quality. An inner potential of 12.5 eV was used in the  $k_z$ -scan analysis (Fig. 7) for the NdNiO<sub>3</sub> film, consistent with previous reports [36]. The same inner potential was used for the Nd<sub>0.6</sub>Sr<sub>1.4</sub>NiO<sub>4</sub>  $k_z$ -scan analysis due to the lack of  $k_z$  dispersion and thus lack of a well-defined periodicity along the axis normal to the sample surface.

#### Results and discussion.

*a. Synthesis, structural characterization, and electrical transport.* We synthesize Nd<sub>2-x</sub>Sr<sub>x</sub>NiO<sub>4</sub> epitaxial thin films on LaAlO<sub>3</sub> ( $x = 0 - 1.4$ ) to traverse the phase diagram previously realized in bulk [28] and thin film [9,20] forms. In Fig. 1(a) we present XRD patterns of the synthesized thin films; the XRD patterns exhibit all even-numbered (00 $l$ ) reflections with no evidence of secondary phases. We confirm that the  $x = 1.4$  film is strained to the LaAlO<sub>3</sub> substrate under 0.9% nominal compressive strain (Fig. S2). Furthermore, we calculate the  $c$ -axis lattice constant for each film using a Nelson-Riley fit [33]. The  $c$ -axis lattice constant varies non-monotonically with  $x$ , peaking at  $x = 0.5$  before decreasing with increasing strontium substitution (Fig. S3). A similar trend was observed in bulk Nd<sub>2-x</sub>Sr<sub>x</sub>NiO<sub>4</sub> [8,23]: the initial increase in the lattice parameter has been attributed to the Jahn-Teller activity of Ni<sup>3+</sup>, followed by a decrease in lattice parameter with the transition from  $d_{3z^2-r^2}$  to  $d_{x^2-y^2}$  orbital filling. A cartoon depiction of the ligand field splitting between the 3d orbitals for  $x = 0$  (Ni<sup>2+</sup>) is illustrated in Fig. S4.

We further interrogate the crystal structure using atomic-resolution STEM imaging. HAADF-STEM imaging reveals coherent ordering of the single-layer Ruddlesden-Popper structure, shown schematically in Fig. 1(a), throughout the thickness of the film. The microstructure of the NdSrNiO<sub>4</sub> ( $x = 1$ ) film is shown in Fig. 1(c). While there are regions of reduced crystallinity and antiphase boundaries (Fig. S5), no large-scale phase segregation or secondary phases such as NiO or SrO are observed. These secondary phases can form when attempting to synthesize nickel in a high oxidation state [26]. Furthermore, atomically resolved EDS mapping in Fig. 1(e) demonstrates homogeneous strontium doping through the thickness of the film.

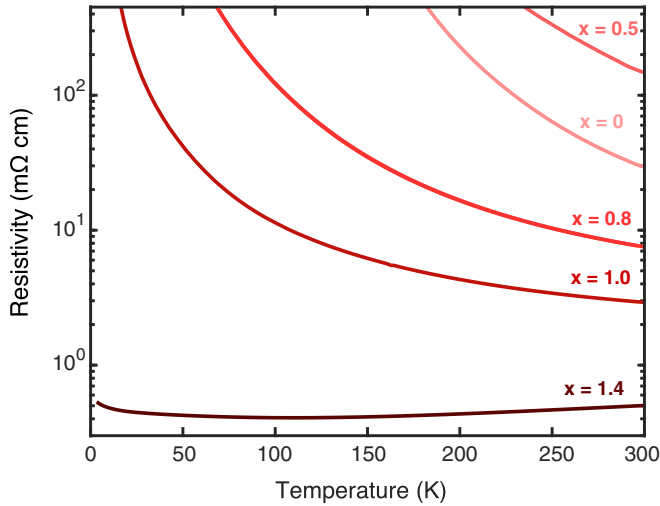


FIG. 2. Electrical transport characterization of  $\text{Nd}_{2-x}\text{Sr}_x\text{NiO}_4$  on  $\text{LaAlO}_3$  ( $x = 0, 0.5, 0.8, 1.0$ , and  $1.4$ ).

Next, we probe the electrical transport of the  $\text{Nd}_{2-x}\text{Sr}_x\text{NiO}_4$  series as a function of strontium doping. As shown in Fig. 2, films with  $x \leq 1.0$  exhibit semiconducting behavior while the  $x = 1.4$  sample is metallic. The resistivity exhibits a nonmonotonic dependence on strontium doping, increasing from  $x = 0$  to  $x = 0.5$  before decreasing for  $x > 0.5$ . This behavior mirrors the variation of the  $c$ -axis lattice constant with strontium doping (Fig. S3), suggesting a potential correlation between resistivity and the Jahn-Teller activity of  $\text{Ni}^{3+}$  at  $x = 0.5$ . The resistive upturn at  $\sim 110$  K for  $x = 1.4$  is likely due to weak localization effects [9]. These results corroborate the critical doping  $x_c \sim 1$  reported in previous studies [9,23,28].

#### b. Electronic structure.

1. *XAS at the O K edge.* With the synthesis of high-quality thin films of  $\text{Nd}_{2-x}\text{Sr}_x\text{NiO}_4$  that demonstrate bulklike crystal structures and electrical properties, we are poised to probe the electronic structure across the series. We use XAS at the O K edge (Fig. 3) to probe the nickel valence and the distribution of holes in the  $e_g$  orbitals between the O  $2p$  and Ni  $3d$  states. Nominally, the O K x-ray absorption spectra can be separated into two regions, the x-ray absorption fine structure (XAFS) and the extended x-ray absorption fine structure (EXAFS) regions. The XANES region encompasses the pre-edge peak centered around 526 – 527 eV, as shown in Fig. 3(a). The pre-edge region corresponds to the excitation of the O  $1s$  electrons to the hybridized O  $2p$  – Ni  $3d$  states. The EXAFS region encompasses the primary spectral region from 530 to 550 eV (see Fig. S6 of the Supplemental Material [37]), which corresponds to the excitation of O  $1s$  electrons to O  $2p$  states hybridized with Nd  $5d$  and Ni  $4sp$  states [38]. However, there is an additional parasitic contribution from the O K-edge signal from the  $\text{LaAlO}_3$  substrate that makes interpreting the EXAFS fine structure complex. We therefore focus solely on the pre-edge feature across the  $\text{Nd}_{2-x}\text{Sr}_x\text{NiO}_4$  series since this region does not have any contributions from the  $\text{LaAlO}_3$  substrate.

We employ polarization-dependent XAS at the O K edge. As shown schematically in Fig. 3(b), polarization-dependent

XAS is a powerful probe to determine the orbital occupancy of the nickel  $3d$  electrons. X-rays with the electric field ( $\mathbf{E}$ ) in-plane ( $\mathbf{E} \parallel a, b$ ) probe the Ni  $d_{x^2-y^2}$  orbital which is hybridized with the O  $2p_x$  and O  $2p_y$  orbitals. Likewise, out-of-plane polarized x-rays ( $\mathbf{E} \parallel c$ ) probe the Ni  $d_{3z^2-r^2}$  orbital that is hybridized with the O  $2p_z$  orbital. In Fig. 3(a), we plot the pre-edge peak of the polarization-dependent O K spectra using  $\text{NdNiO}_3$  as a  $\text{Ni}^{3+}$  reference. As  $x$  increases, the pre-edge peak intensity increases dramatically, accompanied by an enhancement in the XLD signal, as shown in Fig. 3(c). The peak position also shifts to lower energy, consistent with an increase in the nickel valence [39].

In Fig. 3(d), we use Gaussian fits to analyze the pre-edge features of the O K spectra. As the hybridization between Ni  $3d$  and O  $2p$  states is enhanced with hole doping, new transitions are observed in the spectra [22,38,40]. Nominally, we expect the electronic structure to evolve from a dominant  $3d^8$  configuration in the  $\text{Nd}_2\text{NiO}_4$  compound to a mixed  $3d^7 + 3d^8\bar{L}$  configuration for  $\text{NdSrNiO}_4$  ( $x \leq 1.0$ ) and a mixed  $3d^6 + 3d^7\bar{L}$  configuration for  $x = 1.4$  [23,24]. Using the  $\text{NdNiO}_3$  as a nominal  $3d^7$  reference, we find that  $x = 1.0$  in both polarization-dependent spectra looks similar to the  $x = 0.5$  spectra, where we see only two Gaussian peaks which can be ascribed to primarily  $3d^8$  states with a slight admixture of  $3d^7$  and  $3d^8\bar{L}$  configurations. We would expect the  $x = 1.0$  to display an electronic transition from a primarily  $3d^8$  state to an admixture of  $3d^7$  and  $3d^8\bar{L}$  states, synonymous with a  $\text{Ni}^{3+}$  valence state [20,23] [see Fig. S7(a) for the computed peak shifts relative to the  $\text{NdNiO}_3$  reference]. In contrast, the Gaussian fit for  $x = 1.4$  far exceeds the  $3d^7$  electronic transition displaying peaks corresponding to  $\text{Ni}^{3+}$  states (both  $d_{x^2-y^2}$  and  $d_{3z^2-r^2}$  orbitals) and  $\text{Ni}^{4+}$  states. There is a prominent Gaussian peak that shifts to lower energy than in the  $\mathbf{E} \parallel a, b$  polarization spectra, signifying that some of the excess doped holes for  $x > 1.0$ , are preferentially doped into the  $d_{3z^2-r^2}$  orbital [20,23,24,24]. The transition from a dominant ground state  $3d^8$  to a mixture involving  $3d^7$  states for  $x \leq 1.0$  and  $3d^6$  states for  $x = 1.4$ , reflects the complex interplay between the Ni  $3d$  and O  $2p$  hybridized states.

While our spectroscopic signal indicates an increase in nickel valence with hole doping, we can further track the orbital occupancy of these holes and the extent of nickel-oxygen orbital hybridization using the hybridization parameter [38,41]. The hybridization parameter ( $|\beta|^2$ ) relates to the total hole occupation in the  $e_g$  and  $t_{2g}$  orbitals [38]; here the  $t_{2g}$  orbitals are fully occupied ( $t_{2g}^6 e_g^{2-x}$ ) and thus its contribution is negligible. Hence, the hybridization parameter can be simplified to  $|\beta|^2 \propto \frac{I}{I_{e_g}}$  [38]. We computed  $I$ , the spectral intensity of the pre-edge peak, by first employing a spline background subtraction to remove the edge jump, and then integrating the area under the pre-edge peak from about 526 eV to 528 eV [see Fig. S7(b) for details on spline fitting]. Likewise, a discussion of our error analysis, including error propagation methods and statistical validation, can be found in the Supplemental Material [37]. Figure 3(e) shows that, on average, with increasing values of  $x$  (decreasing  $3d$  electron count), the hybridization parameter increases: therefore, there is thus a higher concentration of unoccupied states in the  $e_g$  orbital with increased cation substitution,  $x$ , similar to previous findings [22,38,39,42–44].

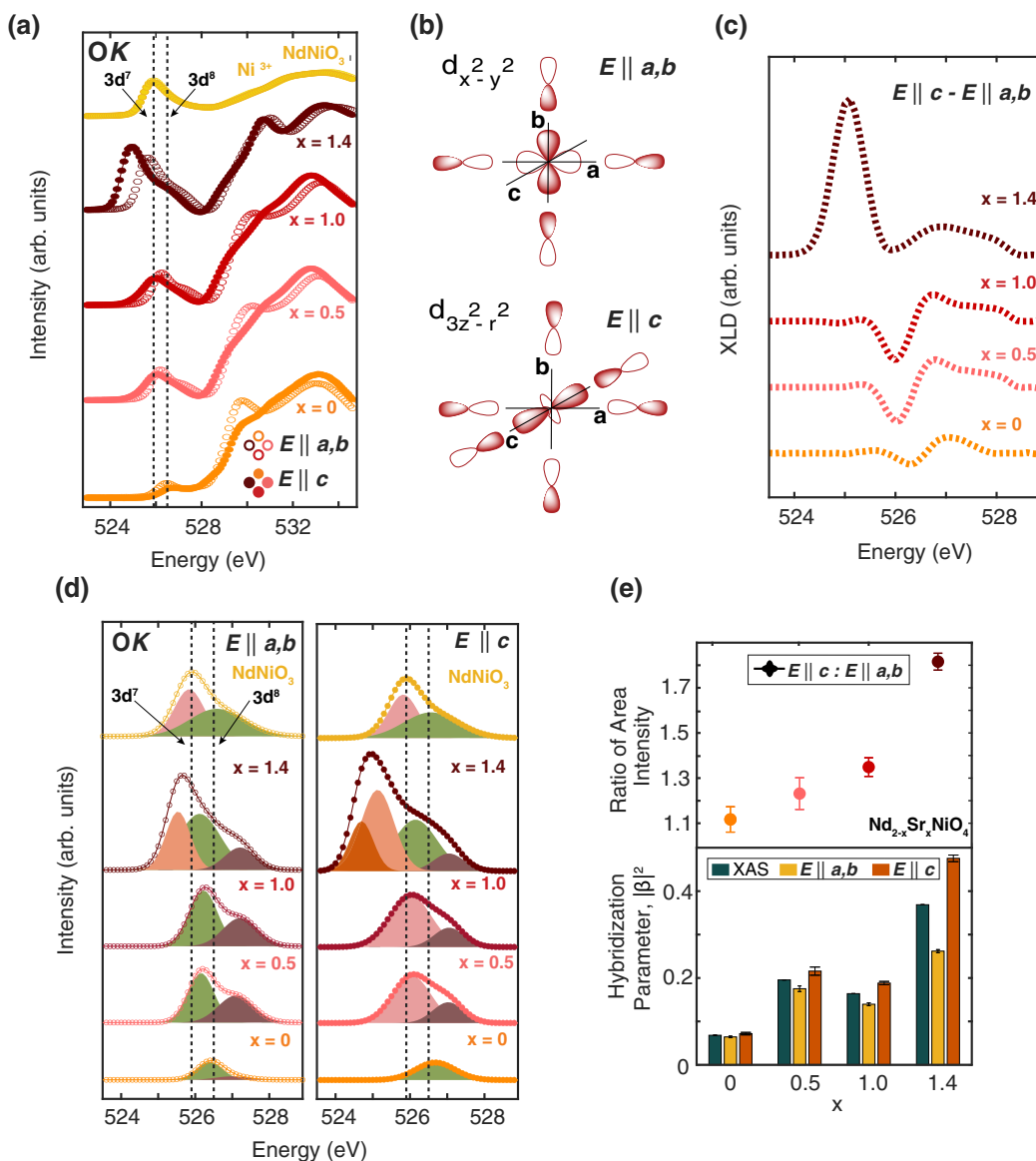


FIG. 3. XAS of  $\text{Nd}_{2-x}\text{Sr}_x\text{NiO}_4$  compounds at the O  $K$  edge. (a) O  $K$  pre-edge peak features in the polarization-averaged, labeled XAS, and polarization-dependent spectra with  $\text{NdNiO}_3$  as a  $\text{Ni}^{3+}$  reference. (b) The in-plane polarized x-rays ( $\mathbf{E} \parallel a, b$ ) are primarily sensitive to the Ni  $d_{x^2-y^2}$  states hybridized with O  $2p_{x,y}$ , whereas the out-of-plane polarized x-rays ( $\mathbf{E} \parallel c$ ) are sensitive to the Ni  $d_{3z^2-r^2}$  states hybridized with O  $2p_z$ . (c) X-ray linear dichroic (XLD) signals. (d) Gaussian fittings of the spectra in (a). The dashed lines represent transitions to nominal  $3d^7$  (left) and  $3d^8$  (right) states. (e) Top: ratio of the out-of-plane ( $\mathbf{E} \parallel c$ ) to in-plane ( $\mathbf{E} \parallel a, b$ ) area intensities across the  $\text{Nd}_{2-x}\text{Sr}_x\text{NiO}_4$  series. Bottom: hybridization parameter for the polarization-dependent and polarization-averaged spectra.

We can further probe the unoccupied states in the respective  $e_g$  orbitals,  $d_{3z^2-r^2}$  and  $d_{x^2-y^2}$ . With increasing  $x$ , the hybridization parameter for both the in-plane and out-of-plane signal increases, as shown in Fig. 3(e). When comparing the signal ratio across the two polarization directions [Fig. 3(e)], we note that on average there are more unoccupied states along the out-of-plane crystallographic direction with  $d_{3z^2-r^2}$  orbital symmetry, indicating preference for holes to align along the out-of-plane crystallographic direction with increasing hole concentration. This trend is consistent with the XLD signal as a function of energy in Fig. 3(c). With increasing  $x$ , we see that the ratio between  $\mathbf{E} \parallel a, b$  and  $\mathbf{E} \parallel c$  decreases. Thus, while at lower doping the holes have an O  $2p_x$  and O  $2p_y$  character, with increasing

hole doping ( $x$ ), the remainder of the holes have O  $2p_z$  character. Overall, we show that as  $x$  increases, the O  $1s - \text{Ni } 3d - \text{O } 2p$  hybridization increases due to the increase in the number of unoccupied  $3d$  states in the  $e_g$  orbitals. More importantly, this increased hybridization indicates strong O  $2p$  character where the holes are highly concentrated on the apical oxygen sites [38,41]. The increase in the pre-edge peak intensity we observe with increasing  $x$  is a trend that is in agreement with many  $R_{2-x}\text{Sr}_x\text{NiO}_4$  single crystals and bulk crystals [10,22,45,46].

2. XAS at the Ni  $L_{2,3}$  edge. Next we analyze the Ni  $L_{2,3}$  edge to assess how hole doping affects the occupation of the  $e_g$  orbitals. We take polarization-dependent spectra at the Ni  $L_{2,3}$  edge, as shown in Fig. 4(a) (see Fig. S8 of the Supplemental

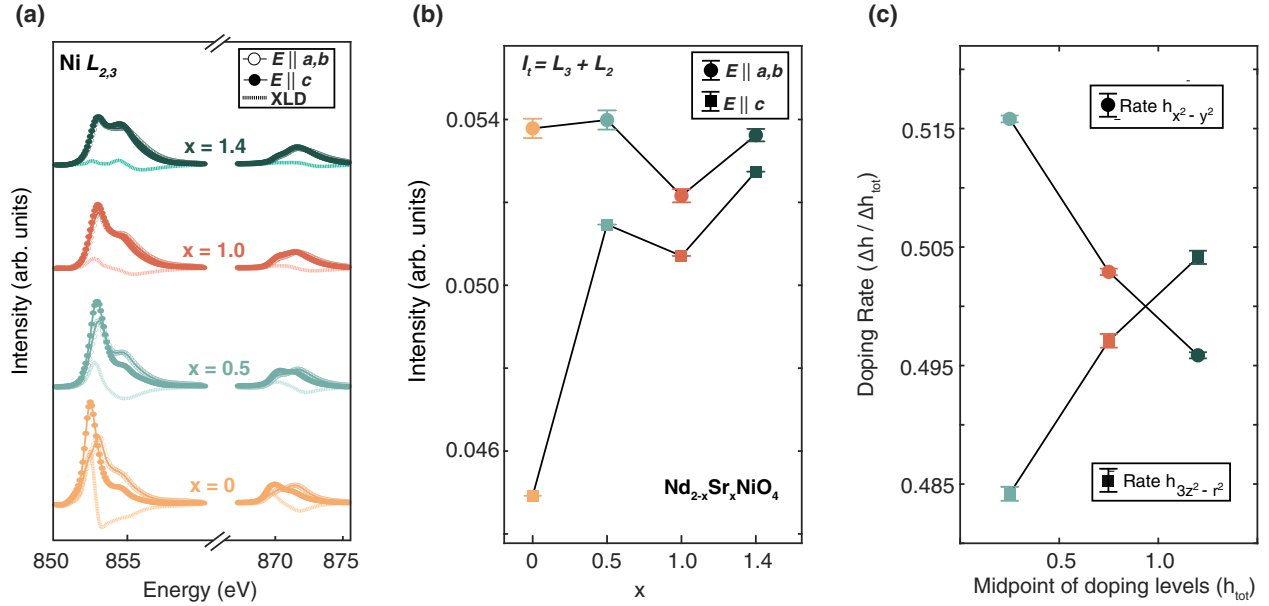


FIG. 4. XAS of  $\text{Nd}_{2-x}\text{Sr}_x\text{NiO}_4$  compounds at the Ni  $L$  edge. (a) Polarization-dependent spectra at the Ni  $L$  edge spectra is presented. Around 852 eV the Ni  $L_3$  edge and its respective linear dichroism is illustrated. Similarly, around 870 eV, the Ni  $L_2$  edge is illustrated along with the Ni  $L_2$  linear dichroism. (b) The total integrated intensity,  $I_t$ , across the Ni  $L$ -edge is computed for  $x = 0$ ,  $x = 0.5$ ,  $x = 1.0$ , and  $x = 1.4$ . More specifically,  $I_t$  is computed for the in-plane ( $\mathbf{E} \parallel a, b$ ) and out-of-plane ( $\mathbf{E} \parallel c$ ) polarization directions. (c) Hole-doping rate into the  $e_g$  orbitals,  $d_{x^2-y^2}$  and  $d_{3z^2-r^2}$ . The data points are plotted at the midpoints of the doping intervals to represent the rate of change between doping levels. The error bars were computed by propagating the uncertainties in the doping rate calculations (see Sec. B in the Supplemental Materials [37]).

Material [37] for the full Ni  $L_{2,3}$  edge before data processing). A large XLD signal is observed for  $x < 1$  and negligible dichroism for  $x > 1$ .

To quantitatively analyze the observed dichroism, we apply the sum rule for linear dichroism [47–49] which relates the ratio of holes in the Ni  $e_g$  orbitals,  $d_{3z^2-y^2}$  and  $d_{x^2-y^2}$ , to the energy-integrated x-ray absorption spectra intensities across the Ni  $L_{2,3}$  edge. The integrated polarization and the polarization-averaged intensities are measured at the Ni  $L_3$  and the Ni  $L_2$  edges with the electric field aligned parallel ( $\mathbf{E} \parallel a, b$ ) and perpendicular ( $\mathbf{E} \parallel c$ ) to the in-plane directions. The hole occupation ratio is defined as

$$R = \frac{h_{3z^2-r^2}}{h_{x^2-y^2}} = \frac{3I_{E\parallel c}}{4I_{E\parallel ab} - I_{E\parallel c}}, \quad (1)$$

where  $h_{3z^2-r^2}$  and  $h_{x^2-y^2}$  are the hole occupation numbers in the  $d_{3z^2-y^2}$  and  $d_{x^2-y^2}$  orbitals, respectively [23]. Equal hole occupation in the  $e_g$  orbitals is represented by  $R = 1$  while 100%  $d_{x^2-y^2}$  character is represented by  $R = 0$ . In Fig. S9, we present the hole occupation and hole occupation ratio in each orbital across the  $\text{Nd}_{2-x}\text{Sr}_x\text{NiO}_4$  series. We observe that as  $x$  increases, holes are increasingly doped into the  $d_{3z^2-r^2}$  orbital, indicating increased nickel-oxygen hybridization with doping. This trend was similarly observed in the O  $K$ -edge spectra in Fig. 3(e). Refer to Fig. S10 of the Supplemental Material [37] for the Ni  $L_{2,3}$  Gaussian peak fits and Figs. S11–S13 for the corresponding error analysis at the Ni  $L_{2,3}$  edge.

We can quantify the difference between the  $\mathbf{E} \parallel a, b$  and  $\mathbf{E} \parallel c$  signals by examining the total integrated intensity of the Ni  $L$  edge spectra in Fig. 4(a). With increasing  $x$ , the difference between the area of the  $\mathbf{E} \parallel c$  and  $\mathbf{E} \parallel a, b$  spectra

decreases, as shown in Fig. 4(b). We then compute the hole doping rate to quantify how holes are introduced into the Ni  $e_g$  orbitals as a function of the total hole count,  $h_{\text{tot}}$ . As shown in Fig. 4(c), the rate of hole occupation increases for  $d_{3z^2-r^2}$  and decreases for  $d_{x^2-y^2}$  with increasing  $x$ . Together, these results suggest that there is a preferential redistribution of holes in the  $d_{3z^2-r^2}$  orbital and enhanced nickel-oxygen hybridization with increasing  $x$ , thus corroborating our observations regarding the hole occupation ratio.

In summary, our XAS results suggest that with increasing values of  $x$ , the holes become more delocalized, resulting in an isotropic distribution of holes across the  $e_g$  orbitals. The increased delocalization of holes is consistent with a more metallic state for larger  $x$ .

*c. ARPES.* We complement the orbital occupancy measurements by characterizing the electronic band structure of the  $\text{Nd}_{2-x}\text{Sr}_x\text{NiO}_4$  films using ARPES. Samples with  $x = 0.8, 1.0$ , and  $1.4$  are investigated, representing semiconducting ( $x = 0.8, 1.0$ ) and metallic ( $x = 1.4$ ) films. These results are compared to ARPES data for the related  $\text{Eu}_{0.9}\text{Sr}_{1.1}\text{NiO}_4$  compound within the same  $\text{R}_{2-x}\text{Sr}_x\text{NiO}_4$  family [10,28].

Constant-energy cuts at the Fermi level in the  $\Gamma - X - M$  plane for the series are shown in Figs. 5(a)–5(c). The Fermi surface, illustrated schematically in Fig. 5(d), consists of an electron pocket of predominantly  $d_{3z^2-r^2}$  character centered at  $\Gamma$  and a hole pocket of largely  $d_{x^2-y^2}$  character centered at  $M$ , consistent with DFT calculations for hole-doped  $\text{Eu}_2\text{NiO}_4$  [10] and paramagnetic  $\text{La}_2\text{NiO}_4$  [27]. As the strontium concentration increases across the series, the signal at the Fermi level increases and the Fermi surface contours in the constant energy cuts become sharper. A similar enhancement

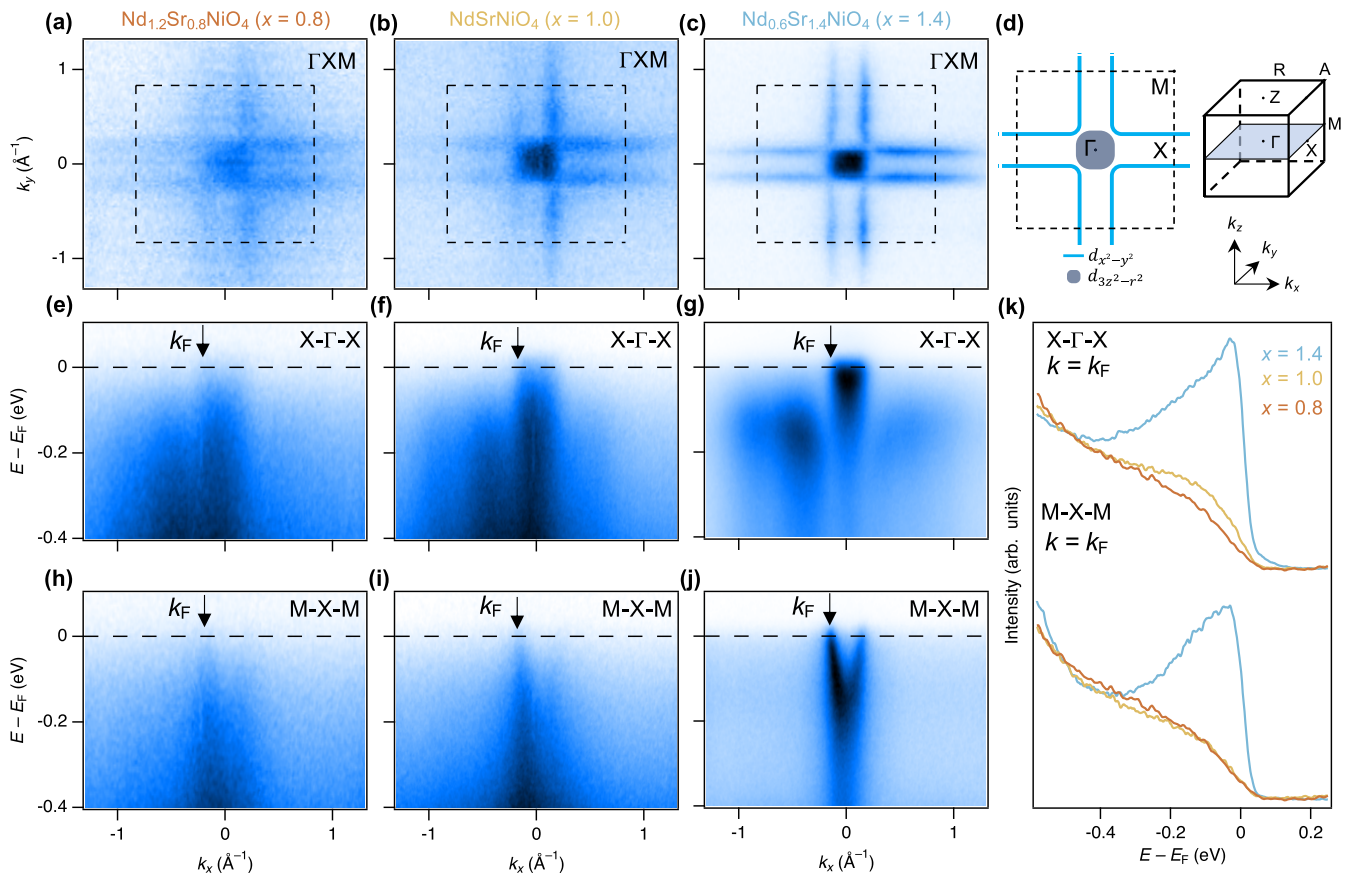


FIG. 5. ARPES characterization of the  $\text{Nd}_{2-x}\text{Sr}_x\text{NiO}_4$  electronic structure. Constant energy cuts at the Fermi energy for (a)  $x = 0.8$ , (b)  $x = 1.0$ , and (c)  $x = 1.4$  measured at 20 K and  $h\nu = 135$  eV. (d) Schematics of the Fermi surface in the  $\Gamma$ -X-M plane and the tetragonal Brillouin zone. E vs  $k_{\parallel}$  cuts along X- $\Gamma$ -X for (e)  $x = 0.8$ , (f)  $x = 1.0$ , and (g)  $x = 1.4$ , respectively. Equivalent energy cuts along M-X-M for (h)  $x = 0.8$ , (i)  $x = 1.0$ , and (j)  $x = 1.4$ , respectively. The arrows in the energy cuts (e)-(j) indicate the Fermi momentum,  $k_F$ . (k) EDCs measured at  $k_F$  for X- $\Gamma$ -X and M-X-M. The spectra are normalized at a binding energy of  $-0.5$  eV.

in contrast and sharpness is evident in the X- $\Gamma$ -X and M-X-M cuts in Figs. 5(e)-5(g) and 5(h)-5(j), respectively.

Signatures of the hole and electron pockets are visible across the doping series, allowing us to track doping-dependent changes. We observe an increase (decrease) in hole (electron) pocket size with increasing strontium content, consistent with hole doping (Fig. S14). We note that the extracted hole and electron densities are unreliable for  $x < 1$  due to the absence of a Fermi crossing [Fig. S14(d)]. Only a remnant Fermi surface remains in this doping regime, making the Luttinger theorem inapplicable [50].

The doping-driven insulator-metal transition is reflected in the energy distribution curves (EDCs) at  $k_F$ , shown in Fig. 5(k). In the semiconducting films ( $x = 0.8$  and  $x = 1.0$ ), only a featureless leading edge is present. In contrast, the metallic sample ( $x = 1.4$ ) exhibits a quasiparticle peak. Symmetrized EDCs, which remove effects related to the Fermi-Dirac distribution [51], reveal a gapped density of states for  $x = 0.8$  and  $x = 1.0$  but no gap for  $x = 1.4$  (Fig. S15). These findings corroborate a critical doping of  $x_c \sim 1$  shown via electrical transport in Fig. 2 and reported in other  $R_{2-x}\text{Sr}_x\text{NiO}_4$  systems [9,10,23,28].

While the transport behavior of our films aligns with bulk  $R_{2-x}\text{Sr}_x\text{NiO}_4$  compounds [9,10,23,28], a key difference

emerges in the momentum-dependence of the EDC line-shapes. In  $\text{Eu}_{0.9}\text{Sr}_{1.1}\text{NiO}_4$ , an anisotropic gap was observed, characterized by a quasiparticle peak in the  $(\pi, \pi)$  direction and a gap gradually opening toward  $(\pi, 0)$  [10]. The metallic state in this system was interpreted as an analog to the pseudogap phase in cuprates [52]. By contrast, our analysis shows negligible momentum dependence across all doping levels (Fig. 6). We take EDCs on the Fermi surface points shown in Fig. 6(a) and find that the EDCs for a given doping are nearly superimposable for the entire doping series. These results suggest that the insulating phase at low doping arises from carrier depletion at the Fermi level, similar to the low temperature insulating state in  $\text{NdNiO}_3$  [53], rather than from a pseudogap phase as seen in cuprates.

Finally, we characterize the electronic dimensionality of  $\text{Nd}_{0.6}\text{Sr}_{1.4}\text{NiO}_4$  [Fig. 7(a)]. We compare the electronic structure of this quasi-two-dimensional compound to the three-dimensional perovskite,  $\text{NdNiO}_3$  [Fig. 7(f)]. Figures 7(b) and 7(c) show the Fermi surfaces of  $\text{NdNiO}_3$  (in the metallic phase above the metal-insulator transition temperature) in the  $\Gamma$ -X-M and Z-R-A plane, respectively. The Fermi surfaces appear qualitatively different in the two planes, consistent with previous literature [36,53]. The  $\text{Nd}_{0.6}\text{Sr}_{1.4}\text{NiO}_4$  Fermi surface in the  $\Gamma$ -X-M plane [Fig. 7(g)], on the other hand,

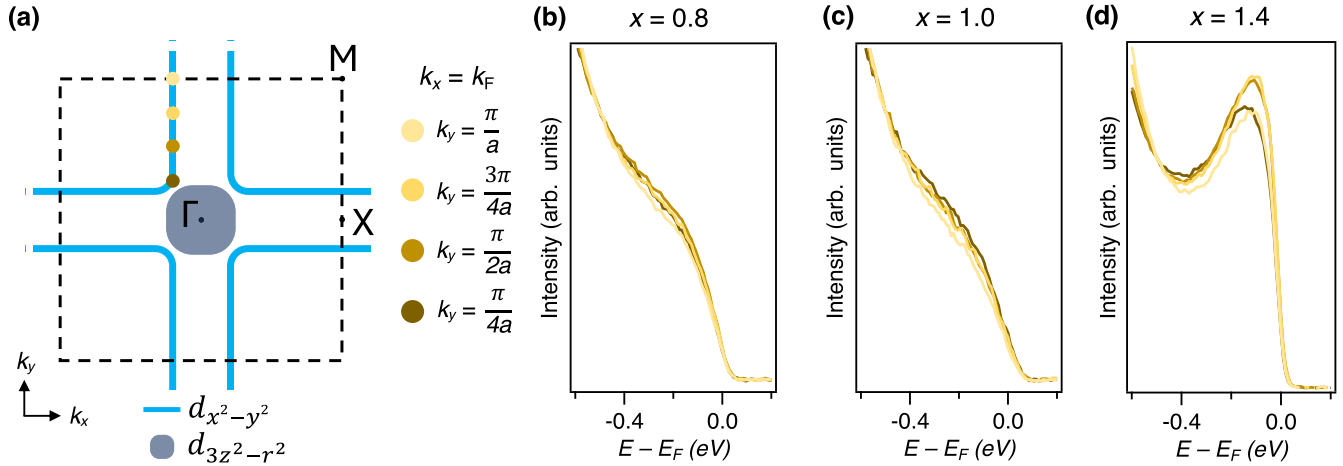


FIG. 6. Investigating the pseudogap via momentum-dependent energy distribution curves (EDCs). (a) Schematic representation of the  $\text{Nd}_{2-x}\text{Sr}_x\text{NiO}_4$  Fermi surface highlighting the points on the Fermi surface where the EDCs in (b)–(d) are extracted. EDCs for (b)  $x = 0.8$ , (c)  $x = 1.0$ , and (d)  $x = 1.4$ , normalized at  $-0.5$  eV.

appears similar to the Z-R-A cut [Fig. 7(h)], pointing to a highly two-dimensional electronic structure.

We directly assess the  $k_z$  dispersion by tuning the incident photon energy to produce  $k_z$  scans. Figures 7(d), 7(i), 7(e), and 7(j) display  $k_z - k_x$  cuts in the  $\Gamma$ -X-Z and X-M-A planes, respectively. Due to the pseudocubic symmetry of the  $\text{NdNiO}_3$  crystal structure, the  $\Gamma$ -X-M (Z-R-A) cut should, in principle, resemble the  $\Gamma$ -X-Z (X-M-A) cut. Indeed, we observe the electron pocket centered at  $\Gamma$  in Fig. 7(d) and the hole pockets centered at M in Fig. 7(e). (We note that  $k_z$  scans typically exhibit lower data quality than scans taken at constant photon energy due to a more coarse sampling of reciprocal space and  $k_z$ -broadening effects [54]). The equivalent Fermi surfaces in

$\text{Nd}_{0.6}\text{Sr}_{1.4}\text{NiO}_4$ , on the other hand, exhibit no  $k_z$  dispersion and intensity modulation only with varying excitation energy [Figs. 7(i) and 7(j)]. The  $\text{Nd}_{0.6}\text{Sr}_{1.4}\text{NiO}_4$  electronic structure is thus fully two-dimensional with no measurable  $k_z$  dispersion. This is at odds with theoretical calculations [10] and ARPES data [28] reported for  $\text{Eu}_{0.9}\text{Sr}_{1.1}\text{NiO}_4$ , where the electron pocket at the  $\Gamma$  point exhibits  $k_z$  dispersion, a feature reminiscent of the three-dimensional electron pocket in  $\text{NdNiO}_3$  [Fig. 7(d)] or  $\text{LaNiO}_3$  [55].

The discrepancy in the electronic dispersion between  $\text{Nd}_{0.6}\text{Sr}_{1.4}\text{NiO}_4$  and  $\text{Eu}_{0.9}\text{Sr}_{1.1}\text{NiO}_4$  is likely unrelated to structural or compositional differences. The structural differences between bulk  $\text{Eu}_{0.9}\text{Sr}_{1.1}\text{NiO}_4$  ( $a = 3.78$  Å,  $c = 12.18$  Å

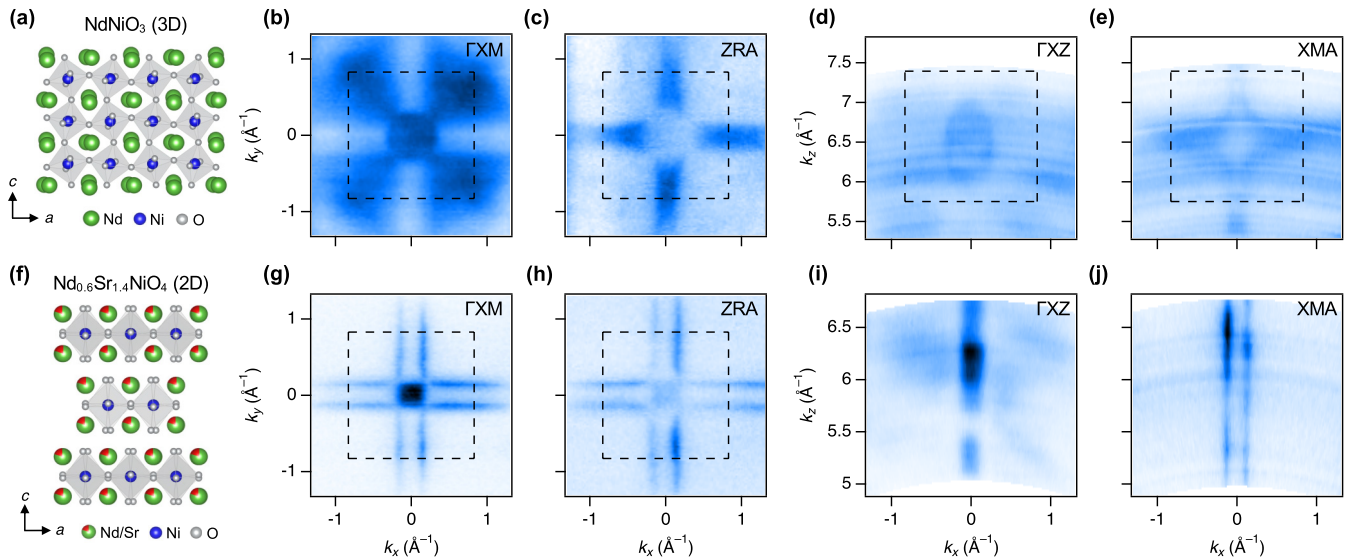


FIG. 7. Characterization of the electronic dimensionality of (a)–(e)  $\text{NdNiO}_3$  and (f–j)  $\text{Nd}_{0.6}\text{Sr}_{1.4}\text{NiO}_4$ . (a), (f) Schematic crystal structures of  $\text{NdNiO}_3$  and  $\text{Nd}_{0.6}\text{Sr}_{1.4}\text{NiO}_4$ , respectively. (b), (g) Fermi surface maps in the  $\Gamma$ -X-M plane taken at 156 eV and 135 eV photon energies, respectively. The  $\Gamma$ -X-M plane in  $\text{NdNiO}_3$  was probed using a 156 eV photon energy in Ref. [36]. (c), (h) Fermi surface maps in the Z-R-A plane taken at 135 eV and 106 eV photon energies, respectively. These photon energies were identified by using the  $\text{NdNiO}_3$  inner potential and the  $\text{Nd}_{0.6}\text{Sr}_{1.4}\text{NiO}_4$  Brillouin zone size in  $k_z$ . Photon energy scans in the (d), (i)  $\Gamma$ -X-Z and (e), (j) X-M-A planes. The dashed squares denote the Brillouin zones. The Brillouin zone is not drawn in (i), (j) due to the impossibility of identifying an inner potential.

[56]) and thin film  $\text{Nd}_{0.6}\text{Sr}_{1.4}\text{NiO}_4$  on  $\text{LaAlO}_3$  ( $a = 3.79 \text{ \AA}$ ,  $c = 12.34 \text{ \AA}$ , from Fig. S3) are small and unlikely to account for a significant variation in electronic dimensionality. Furthermore, prior studies indicate that the  $R_{2-x}\text{Sr}_x\text{NiO}_4$  phase diagram is relatively insensitive to the rare-earth  $R$  [14,46,57,58], suggesting that the difference in rare-earth elements, or their valence state, are unlikely to account for the distinct electronic dispersion between  $\text{Eu}_{2-x}\text{Sr}_x\text{NiO}_4$  and  $\text{Nd}_{2-x}\text{Sr}_x\text{NiO}_4$ .

Given the minimal rare-earth dependence in  $R_{2-x}\text{Sr}_x\text{NiO}_4$  compounds, it is intriguing that first principle calculations predict a fully two-dimensional electronic structure for paramagnetic  $\text{La}_2\text{NiO}_4$  [27], yet a distinctly three-dimensional one for  $\text{Eu}_{2-x}\text{Sr}_x\text{NiO}_4$  [10,28]. Notably, quasi-2D Ruddlesden-Popper compounds can still exhibit a three-dimensional Fermi surface. For example, the cuprate  $\text{La}_{2-x}\text{Sr}_x\text{CuO}_4$ , which is isostructural to  $R_{2-x}\text{Sr}_x\text{NiO}_4$ , exhibits non-negligible  $k_z$  dispersion at the antinode [59]. Like its nickelate counterpart,  $\text{La}_{2-x}\text{Sr}_x\text{CuO}_4$  shows minimal variation in electronic properties with rare-earth substitution (neodymium and europium for lanthanum) [60,61]. Further experimental and theoretical work is needed to clarify the origin of  $k_z$  dispersion in quasi-2D  $R_{2-x}\text{Sr}_x\text{NiO}_4$  compounds.

**Conclusions.** We synthesized  $\text{Nd}_{2-x}\text{Sr}_x\text{NiO}_4$  thin films on  $\text{LaAlO}_3$  via ozone-assisted MBE and characterized their electrical properties. Our results reveal a doping-driven insulator-to-metal transition at  $x_c \sim 1$ , consistent with previous studies of both bulk [28,58] and thin-film [9,20] compounds. Using polarization-dependent XAS, we track the evolution of the electronic structure with hole doping. With increased hole doping we observe an increase in the nickel valence, coupled with an increase in the covalency between the O  $2p$  states and the Ni  $3d$  states. There is a particularly pronounced increase in hole occupation with O  $2p_z - \text{Ni } 3z^2 - r^2$  character with hole doping. This delocalization of holes is further corroborated with the analysis of the Ni  $L_{2,3}$ -edge spectra. Finally, we complement the orbital-dependent XAS measurements with ARPES measurements of the electronic structure. The Fermi surface we observe via ARPES consists of a large hole pocket of  $d_{x^2-y^2}$  character centered at M along with an electron pocket of  $d_{3z^2-r^2}$  character at  $\Gamma$ , qualitatively consistent with the paramagnetic  $\text{La}_2\text{NiO}_4$  Fermi surface calculated via DFT. However, in contrast to previous data on bulk  $\text{Eu}_{0.9}\text{Sr}_{1.1}\text{NiO}_4$  [28], we do not observe a cupratelike momentum-dependent pseudogap or  $k_z$  dispersion of the electron or hole pockets.

**Acknowledgments.** We thank S. Smith for feedback on the manuscript. Research is primarily supported by the U.S. Department of Energy (DOE), Office of Basic Energy Sciences, Division of Materials Sciences and Engineering, under Award No. DE-SC0021925. This work used resources of the Advanced Light Source, which is a DOE Office of Science User Facility under Contract No. DE-AC02-05CH11231. The ARPES work was supported by the U.S. Department of Energy, Office of Science, Office of Basic Energy Sciences, Materials Sciences and Engineering Division, under Contract No. DE-AC02-05-CH11231 within the Ultrafast Materials Science Program No. KC2203. Device fabrication work was performed at Harvard University's Center for Nanoscale Systems (CNS), a member of the National Nanotechnology Coordinated Infrastructure Network (NNCI), supported by the National Science Foundation under NSF Grant No. 1541959. Electron microscopy was carried out through the use of MIT.nano facilities at the Massachusetts Institute of Technology. N.K.T. acknowledges the support of a Ford Foundation Predoctoral Fellowship and the support from the ALS Doctoral Fellowship in Residence. D.F.S. and G.A.P. acknowledges support from the NSF Graduate Research Fellowship Grant No. DGE-1745303. G.A.P. acknowledges additional support from the Paul & Daisy Soros Fellowship for New Americans. A.B.T. acknowledges support from the National Science Foundation under Award No. DMR-2323970. J.A.M. acknowledges support from the Packard Foundation and the Sloan Foundation. Y.Z. and I.E. were supported by The Rowland Institute at Harvard.

N.K.T., D.F.S., A.B.T., G.A.P., C.M.B., and J.A.M. synthesized the thin films. N.K.T., D.F.S., S.T.D., and J.A.M. performed the electrical measurements. Y.Z. and I.E.B. characterized the samples with scanning transmission electron microscopy. S.D., N.K.T., and A.T.N. performed x-ray spectroscopy measurements. N.K.T. analyzed the x-ray spectroscopy data with discussion from G.A.P. ARPES data were acquired by D.F.S., H.J., and L.M. with assistance from A.B., C.J., E.R., and A.L. D.F.S. and L.M. analyzed the ARPES data. J.A.M. conceived and guided the study. N.K.T., D.F.S., and J.A.M. wrote the manuscript with discussion and contributions from all authors.

The authors declare no competing interests.

**Data availability.** The data that support the findings of this study are available from the corresponding authors upon reasonable request.

- 
- [1] P. Ganguly and C. Rao, Crystal chemistry and magnetic properties of layered metal oxides possessing the  $\text{K}_2\text{NiF}_4$  or related structures, *J. Solid State Chem.* **53**, 193 (1984).
- [2] R. J. Cava, B. Batlogg, T. T. Palstra, J. J. Krajewski, W. F. Peck, A. P. Ramirez, and L. W. Rupp, Magnetic and electrical properties of  $\text{La}_{2-x}\text{Sr}_x\text{NiO}_{4\pm\delta}$ , *Phys. Rev. B* **43**, 1229 (1991).
- [3] C. H. Chen, S.-W. Cheong, and A. S. Cooper, Charge modulations in  $\text{La}_{2-x}\text{Sr}_x\text{NiO}_{4+y}$ : Ordering of polarons, *Phys. Rev. Lett.* **71**, 2461 (1993).
- [4] S. Chen, K. Ramanujachary, and M. Greenblatt, Investigations on the structural, electrical and magnetic properties of R substituted  $\text{Ln}_2\text{NiO}_4$  ( $\text{Ln} = \text{Pr}, \text{Sm}, \text{Gd}$ ), *J. Solid State Chem.* **105**, 444 (1993).
- [5] V. I. Anisimov, D. Bukhvalov, and T. M. Rice, Electronic structure of possible nickelate analogs to the cuprates, *Phys. Rev. B* **59**, 7901 (1999).
- [6] R. Markiewicz, A survey of the Van Hove scenario for high- $T_c$  superconductivity with special emphasis on pseudogaps and striped phases, *J. Phys. Chem. Solids* **58**, 1179 (1997).

- [7] J. G. Bednorz, K. A. Müller, and M. Takashige, Superconductivity in alkaline earth-substituted  $\text{La}_2\text{CuO}_{4-y}$ , *Science* **236**, 73 (1987).
- [8] Y. Takeda, M. Nishijima, N. Imanishi, R. Kanno, O. Yamamoto, and M. Takano, Crystal chemistry and transport properties of  $\text{Nd}_{2-x}\text{A}_x\text{NiO}_4$  ( $A = \text{Ca}, \text{Sr}, \text{or Ba}, 0 \leq x \leq 1.4$ ), *J. Solid State Chem.* **96**, 72 (1992).
- [9] S. Shinomori, Y. Okimoto, M. Kawasaki, and Y. Tokura, Insulator–metal transition in  $\text{La}_{2-x}\text{Sr}_x\text{NiO}_4$ , *J. Phys. Soc. Jpn.* **71**, 705 (2002).
- [10] M. Uchida, K. Ishizaka, P. Hansmann, Y. Kaneko, Y. Ishida, X. Yang, R. Kumai, A. Toschi, Y. Onose, R. Arita, K. Held, O. K. Andersen, S. Shin, and Y. Tokura, Pseudogap of metallic layered nickelate  $\text{R}_{2-x}\text{Sr}_x\text{NiO}_4$  ( $R = \text{Nd}, \text{Eu}$ ) crystals measured using angle-resolved photoemission spectroscopy, *Phys. Rev. Lett.* **106**, 027001 (2011).
- [11] S.-W. Cheong, H. Y. Hwang, C. H. Chen, B. Batlogg, L. W. Rupp, and S. A. Carter, Charge-ordered states in  $(\text{La}, \text{Sr})_2\text{NiO}_4$  for hole concentrations  $n_h = 1/3$  and  $1/2$ , *Phys. Rev. B* **49**, 7088 (1994).
- [12] S. Anissimova, D. Parshall, G. Gu, K. Marty, M. Lumsden, S. Chi, J. Fernandez-Baca, D. Abernathy, D. Lamago, J. Tranquada, and D. Reznik, Direct observation of dynamic charge stripes in  $\text{La}_{2-x}\text{Sr}_x\text{NiO}_4$ , *Nat. Commun.* **5**, 3467 (2014).
- [13] H. Yoshizawa, T. Kakeshita, R. Kajimoto, T. Tanabe, T. Katsufuji, and Y. Tokura, Stripe order at low temperatures in  $\text{La}_{2-x}\text{Sr}_x\text{NiO}_4$  with  $0.289 \leq x \leq 0.5$ , *Phys. Rev. B* **61**, R854 (2000).
- [14] R. Kajimoto, K. Ishizaka, H. Yoshizawa, and Y. Tokura, Spontaneous rearrangement of the checkerboard charge order to stripe order in  $\text{La}_{1.5}\text{Sr}_{0.5}\text{NiO}_4$ , *Phys. Rev. B* **67**, 014511 (2003).
- [15] X. L. Wang, C. Stassis, D. C. Johnston, T. C. Leung, J. Ye, B. N. Harmon, G. H. Lander, A. J. Schultz, C.-K. Loong, and J. M. Honig, The antiferromagnetic form factor of  $\text{La}_2\text{NiO}_4$ , *J. Appl. Phys.* **69**, 4860 (1991).
- [16] H. Sun, M. Huo, X. Hu, J. Li, Z. Liu, Y. Han, L. Tang, Z. Mao, P. Yang, B. Wang, J. Cheng, D.-X. Yao, G.-M. Zhang, and M. Wang, Signatures of superconductivity near 80 K in a nickelate under high pressure, *Nature (London)* **621**, 493 (2023).
- [17] F. Baiutti, G. Christiani, and G. Logvenov, Towards precise defect control in layered oxide structures by using oxide molecular beam epitaxy, *Beilstein J. Nanotechnol.* **5**, 596 (2014).
- [18] I. Božović, G. Logvenov, and V. Butko, Atomic-layer engineering of nickelates (in search of novel superconductors), *Physica C* **615**, 1354388 (2023).
- [19] S. Catalano, M. Gibert, J. Fowlie, J. ñiguez, J.-M. Triscone, and J. Kreisel, Rare-earth nickelates  $\text{RNiO}_3$ : thin films and heterostructures, *Rep. Prog. Phys.* **81**, 046501 (2018).
- [20] A. Sahiner, M. Croft, Z. Zhang, M. Greenblatt, I. Perez, P. Metcalf, H. Jhans, G. Liang, and Y. Jeon, Electronic structure anisotropy and  $d$ -configuration in Ni-based materials, *Phys. Rev. B* **53**, 9745 (1996).
- [21] A. Tiwari, C. Jin, and J. Narayan, Strain-induced tuning of metal–insulator transition in  $\text{NdNiO}_3$ , *Appl. Phys. Lett.* **80**, 4039 (2002).
- [22] Z. Hu, M. S. Golden, J. Fink, G. Kaindl, S. A. Warda, D. Reinen, P. Mahadevan, and D. D. Sarma, Hole distribution between the Ni  $3d$  and O  $2p$  orbitals in  $\text{Nd}_{2-x}\text{Sr}_x\text{NiO}_{4-\delta}$ , *Phys. Rev. B* **61**, 3739 (2000).
- [23] M. Uchida, Y. Yamasaki, Y. Kaneko, K. Ishizaka, J. Okamoto, H. Nakao, Y. Murakami, and Y. Tokura, Pseudogap-related charge dynamics in the layered nickelate  $\text{R}_{2-x}\text{Sr}_x\text{NiO}_4$  ( $x \approx 1$ ), *Phys. Rev. B* **86**, 165126 (2012).
- [24] E. Pellegrin, J. Zaanen, H.-J. Lin, G. Meigs, C. T. Chen, G. H. Ho, H. Eisaki, and S. Uchida, O  $1s$  near-edge x-ray absorption of  $\text{La}_{2-x}\text{Sr}_x\text{NiO}_{4+\delta}$ : Holes, polarons, and excitons, *Phys. Rev. B* **53**, 10667 (1996).
- [25] P. Kuiper, J. v. Elp, D. E. Rice, D. J. Buttrey, H. J. Lin, and C. T. Chen, Polarization-dependent nickel  $2p$  x-ray-absorption spectra of  $\text{La}_2\text{NiO}_{4+\delta}$ , *Phys. Rev. B* **57**, 1552 (1998).
- [26] L. Wang, Z. Yang, X. Yin, S. D. Taylor, X. He, C. S. Tang, M. E. Bowden, J. Zhao, J. Wang, J. Liu, D. E. Perea, L. Wangoh, A. T. S. Wee, H. Zhou, S. A. Chambers, and Y. Du, Spontaneous phase segregation of  $\text{Sr}_2\text{NiO}_3$  and  $\text{SrNi}_2\text{O}_3$  during  $\text{SrNiO}_3$  heteroepitaxy, *Sci. Adv.* **7**, eabe2866 (2021).
- [27] A. S. Botana and M. R. Norman, Layered palladates and their relation to nickelates and cuprates, *Phys. Rev. Mater.* **2**, 104803 (2018).
- [28] M. Uchida, K. Ishizaka, P. Hansmann, X. Yang, M. Sakano, J. Miyawaki, R. Arita, Y. Kaneko, Y. Takata, M. Oura, A. Toschi, K. Held, A. Chainani, O. K. Andersen, S. Shin, and Y. Tokura, Orbital characters of three-dimensional Fermi surfaces in  $\text{Eu}_{2-x}\text{Sr}_x\text{NiO}_4$  as probed by soft-x-ray angle-resolved photoemission spectroscopy, *Phys. Rev. B* **84**, 241109(R) (2011).
- [29] G. A. Pan, Q. Song, D. F. Segedin, M.-C. Jung, H. El-Sherif, E. E. Fleck, B. H. Goodge, S. Doyle, D. C. Carrizales, A. T. N'Diaye, P. Shafer, H. Paik, L. F. Kourkoutis, I. E. Baggari, A. S. Botana, C. M. Brooks, and J. A. Mundy, Synthesis and electronic properties of  $\text{Nd}_{n+1}\text{Ni}_n\text{O}_{3n+1}$  Ruddlesden-Popper nickelate thin films, *Phys. Rev. Mater.* **6**, 055003 (2022).
- [30] W. Sun, Y. Li, X. Cai, J. Yang, W. Guo, Z. Gu, Y. Zhu, and Y. Nie, Electronic and transport properties in Ruddlesden-Popper neodymium nickelates  $\text{Nd}_{n+1}\text{Ni}_n\text{O}_{3n+1}$  ( $n = 1 - 5$ ), *Phys. Rev. B* **104**, 184518 (2021).
- [31] Z. Li, W. Guo, T. T. Zhang, J. H. Song, T. Y. Gao, Z. B. Gu, and Y. F. Nie, Epitaxial growth and electronic structure of Ruddlesden–Popper nickelates  $(\text{La}_{n+1}\text{Ni}_n\text{O}_{3n+1}, n = 1 - 5)$ , *APL Mater.* **8**, 091112 (2020).
- [32] C. M. Brooks, L. F. Kourkoutis, T. Heeg, J. Schubert, D. A. Muller, and D. G. Schlom, Growth of homoepitaxial  $\text{SrTiO}_3$  thin films by molecular-beam epitaxy, *Appl. Phys. Lett.* **94**, 162905 (2009).
- [33] J. B. Nelson and D. P. Riley, An experimental investigation of extrapolation methods in the derivation of accurate unit-cell dimensions of crystals, *Proc. Phys. Soc.* **57**, 160 (1945).
- [34] B. H. Savitzky, I. El Baggari, C. B. Clement, E. Waite, B. H. Goodge, D. J. Baek, J. P. Sheckelton, C. Pasco, H. Nair, N. J. Schreiber, J. Hoffman, A. S. Admasu, J. Kim, S.-W. Cheong, A. Bhattacharya, D. G. Schlom, T. M. McQueen, R. Hovden, and L. F. Kourkoutis, Image registration of low signal-to-noise cryo-stem data, *Ultramicroscopy* **191**, 56 (2018).
- [35] W. Wu, D. Huang, G. Guo, H.-J. Lin, T. Hou, C. Chang, C. Chen, A. Fujimori, T. Kimura, H. Huang, A. Tanaka, and T. Jo, Orbital polarization of  $\text{LaSrMnO}_4$  studied by soft x-ray linear dichroism, *J. Electron Spectrosc. Relat. Phenom.* **137-140**, 641 (2004).
- [36] Q. Song, S. Doyle, G. A. Pan, I. E. Baggari, D. F. Segedin, D. C. Carrizales, J. Nordlander, C. Tzschaschel, J. R. Ehrets, Z. Hasan, H. El-Sherif, J. Krishna, C. Hanson, H. LaBollita,

- A. Bostwick, C. Jozwiak, E. Rotenberg, S.-Y. Xu, A. Lanzara, A. T. N'Diaye *et al.*, Antiferromagnetic metal phase in an electron-doped rare-earth nickelate, *Nat. Phys.* **19**, 522 (2023).
- [37] See Supplemental Material at <http://link.aps.org/supplemental/10.1103/PhysRevMaterials.9.L032001> for synthesis and electronic characterization of  $\text{Nd}_{2-x}\text{Sr}_x\text{NiO}_4$  thin films ( $0 \leq x \leq 1.4$ ).
- [38] J. Suntivich, W. T. Hong, Y.-L. Lee, J. M. Rondinelli, W. Yang, J. B. Goodenough, B. Dabrowski, J. W. Freeland, and Y. Shao-Horn, Estimating hybridization of transition metal and oxygen states in perovskites from O *K*-edge X-ray absorption spectroscopy, *J. Phys. Chem. C* **118**, 1856 (2014).
- [39] F. Frati, M. O. J. Y. Hunault, and F. M. F. d. Groot, Oxygen *K*-edge X-ray absorption spectra, *Chem. Rev.* **120**, 4056 (2020).
- [40] P. Kuiper, J. v. Elp, G. A. Sawatzky, A. Fujimori, S. Hosoya, and D. M. d. Leeuw, Unoccupied density of states of  $\text{La}_{2-x}\text{Sr}_x\text{NiO}_{4+\delta}$  studied by polarization-dependent x-ray-absorption spectroscopy and bremsstrahlung isochromat spectroscopy, *Phys. Rev. B* **44**, 4570 (1991).
- [41] F. M. F. d. Groot, M. Grioni, J. C. Fuggle, J. Ghijsen, G. A. Sawatzky, and H. Petersen, Oxygen 1s x-ray-absorption edges of transition-metal oxides, *Phys. Rev. B* **40**, 5715 (1989).
- [42] M. Abbate, F. M. F. de Groot, J. C. Fuggle, A. Fujimori, O. Strebel, F. Lopez, M. Domke, G. Kaindl, G. A. Sawatzky, M. Takano, Y. Takeda, H. Eisaki, and S. Uchida, Controlled-valence properties of  $\text{La}_{1-x}\text{Sr}_x\text{FeO}_3$  and  $\text{La}_{1-x}\text{Sr}_x\text{MnO}_3$  studied by soft-x-ray absorption spectroscopy, *Phys. Rev. B* **46**, 4511 (1992).
- [43] O. Toulemonde, N. N'Guyen, F. Studer, and A. Traverse, Spin state transition in  $\text{LaCoO}_3$  with temperature or strontium doping as Seen by XAS, *J. Solid State Chem.* **158**, 208 (2001).
- [44] D. D. Sarma, K. Maiti, E. Vescovo, C. Carbone, W. Eberhardt, O. Rader, and W. Gudat, Investigation of hole-doped insulating  $\text{La}_{1-x}\text{Sr}_x\text{CoO}_3$  by soft-x-ray absorption spectroscopy, *Phys. Rev. B* **53**, 13369 (1996).
- [45] J. Millburn, M. Green, D. Neumann, and M. Rosseinsky, Evolution of the structure of the  $\text{K}_2\text{NiF}_4$  phases  $\text{La}_{2-x}\text{Sr}_x\text{NiO}_{4+\delta}$  with oxidation state: Octahedral distortion and phase separation ( $0.2 \leq x \leq 1.0$ ), *J. Solid State Chem.* **145**, 401 (1999).
- [46] Y. Takeda, R. Kanno, M. Sakano, O. Yamamoto, M. Takano, Y. Bando, H. Akinaga, K. Takita, and J. Goodenough, Crystal chemistry and physical properties of  $\text{La}_{2-x}\text{Sr}_x\text{NiO}_4$  ( $0 \leq x \leq 1.6$ ), *Mater. Res. Bull.* **25**, 293 (1990).
- [47] B. T. Thole and G. v. d. Laan, Sum rules for magnetic dichroism in rare earth 4*f* photoemission, *Phys. Rev. Lett.* **70**, 2499 (1993).
- [48] G. v. d. Laan, Sum rules and fundamental spectra of magnetic x-ray dichroism in crystal field symmetry, *J. Phys. Soc. Jpn.* **63**, 2393 (1994).
- [49] H. Wang, S. Friedrich, L. Li, Z. Mao, P. Ge, M. Balasubramanian, and D. S. Patil, L-edge sum rule analysis on 3d transition metal sites: from  $d^{10}$  to  $d^0$  and towards application to extremely dilute metallo-enzymes, *Phys. Chem. Chem. Phys.* **20**, 8166 (2018).
- [50] F. Ronning, C. Kim, D. L. Feng, D. S. Marshall, A. G. Loeser, L. L. Miller, J. N. Eckstein, I. Bozovic, and Z.-X. Shen, Photoemission evidence for a remnant Fermi surface and a d-wave-like dispersion in insulating  $\text{Ca}_2\text{CuO}_2\text{Cl}_2$ , *Science* **282**, 2067 (1998).
- [51] M. R. Norman, H. Ding, M. Randeria, J. C. Campuzano, T. Yokoya, T. Takeuchi, T. Takahashi, T. Mochiku, K. Kadowaki, P. Guptasarma, and D. G. Hinks, Destruction of the Fermi surface in underdoped high-*T*<sub>c</sub> superconductors, *Nature (London)* **392**, 157 (1998).
- [52] A. A. Kordyuk, Pseudogap from ARPES experiment: Three gaps in cuprates and topological superconductivity (Review Article), *Low Temp. Phys.* **41**, 319 (2015).
- [53] R. S. Dhaka, T. Das, N. C. Plumb, Z. Ristic, W. Kong, C. E. Matt, N. Xu, K. Dolui, E. Razzoli, M. Medarde, L. Patthey, M. Shi, M. Radović, and J. Mesot, Tuning the metal-insulator transition in  $\text{NdNiO}_3$  heterostructures via fermi surface instability and spin fluctuations, *Phys. Rev. B* **92**, 035127 (2015).
- [54] A. Damascelli, Probing the electronic structure of complex systems by ARPES, *Phys. Scr.* **T109**, 61 (2004).
- [55] H. K. Yoo, S. I. Hyun, L. Moreschini, H.-D. Kim, Y. J. Chang, C. H. Sohn, D. W. Jeong, S. Sinn, Y. S. Kim, A. Bostwick, E. Rotenberg, J. H. Shim, and T. W. Noh, Latent instabilities in metallic  $\text{LaNiO}_3$  films by strain control of Fermi-surface topology, *Sci. Rep.* **5**, 8746 (2015).
- [56] L. Hui, C. Ping, G. Yuping, L. Yueqing, L. Guanglie, X. Yuanzhe, and M. Futai, Preparation, crystal structure, and reducibility of  $\text{K}_2\text{NiF}_4$  type oxides  $\text{Eu}_{2-x}\text{Sr}_x\text{Ni}_{4+\delta}$ , *J. Solid State Chem.* **141**, 99 (1998).
- [57] M. Hücker, M. v. Zimmermann, R. Klingeler, S. Kiele, J. Geck, S. N. Bakehe, J. Z. Zhang, J. P. Hill, A. Revcolevschi, D. J. Buttrey, B. Büchner, and J. M. Tranquada, Unidirectional diagonal order and three-dimensional stacking of charge stripes in orthorhombic  $\text{Pr}_{1.6}\text{Sr}_{0.33}\text{NiO}_4$  and  $\text{Nd}_{1.67}\text{Sr}_{0.33}\text{NiO}_4$ , *Phys. Rev. B* **74**, 085112 (2006).
- [58] M. Uchida, *Spectroscopic Study on Charge-Spin-Orbital Coupled Phenomena in Mott-Transition Oxides*, Springer Theses (Springer, 2013).
- [59] M. Horio, K. Hauser, Y. Sassa, Z. Mingazheva, D. Sutter, K. Kramer, A. Cook, E. Nocerino, O. K. Forslund, O. Tjernberg, M. Kobayashi, A. Chikina, N. B. M. Schröter, J. A. Krieger, T. Schmitt, V. N. Strocov, S. Pyon, T. Takayama, H. Takagi, O. J. Lipscombe *et al.*, Three-dimensional Fermi surface of overdoped la-based cuprates, *Phys. Rev. Lett.* **121**, 077004 (2018).
- [60] N. Doiron-Leyraud, O. Cyr-Choinière, S. Badoux, A. Ataei, C. Collignon, A. Gourgout, S. Dufour-Beauséjour, F. F. Tafti, F. Laliberté, M.-E. Boulanger, M. Matusiak, D. Graf, M. Kim, J.-S. Zhou, N. Momono, T. Kurosawa, H. Takagi, and L. Taillefer, Pseudogap phase of cuprate superconductors confined by Fermi surface topology, *Nat. Commun.* **8**, 2044 (2017).
- [61] O. Cyr-Choinière, R. Daou, F. Laliberté, C. Collignon, S. Badoux, D. LeBoeuf, J. Chang, B. J. Ramshaw, D. A. Bonn, W. N. Hardy, R. Liang, J.-Q. Yan, J.-G. Cheng, J.-S. Zhou, J. B. Goodenough, S. Pyon, T. Takayama, H. Takagi, N. Doiron-Leyraud, and L. Taillefer, Pseudogap temperature  $T^*$  of cuprate superconductors from the Nernst effect, *Phys. Rev. B* **97**, 064502 (2018).